Modified Magnus effect and vortex modes of rotating cylinder due to interaction with free surface in two-phase flow

RESEARCH ARTICLE | DECEMBER 27 2023

Modified Magnus effect and vortex modes of rotating cylinder due to interaction with free surface in two-phase flow

Jianfeng Lin (林健峰) ; Hua-Dong Yao (姚华栋)

Physics of Fluids 35, 123614 (2023)
https://doi.org/10.1063/5.0179744

Physics of Fluids ARTICLE pubs.aip.org/aip/pof

Modified Magnus effect and vortex modes of rotating cylinder due to interaction with free surface in two-phase flow

Cite as: Phys. Fluids **35**, 123614 (2023); doi: 10.1063/5.0179744
Submitted: 4 October 2023 · Accepted: 7 December 2023 ·
Published Online: 27 December 2023

Jianfeng Lin (林健峰),[1,2] and Hua-Dong Yao (姚华栋)[1,a)]

AFFILIATIONS

[1]Department of Mechanics and Maritime Sciences, Chalmers University of Technology, 412 96 Gothenburg, Sweden
[2]College of Shipbuilding Engineering, Harbin Engineering University, No. 145 Nantong Street, Nangang District, Harbin 150001, China

[a)]Author to whom correspondence should be addressed: huadong.yao@chalmers.se

ABSTRACT

When employing rotating cylinders as ship anti-rolling devices based on the Magnus effect, the cylinders are near the free surface. However, most of the previous studies on rotating cylinders considered single-phase (SP) flows, where the interaction between the free surface and rotating cylinders was missing. In this study, we explore a rotating cylinder in a two-phase flow using large eddy simulation. Given low submergence depths of less than one cylinder diameter, the pattern of vortices classified as mode A in the SP flow under the same operation conditions is altered to mode E. As regards depths below 1.5 diameters, mode E is changed to mode F′. These modes mentioned above were defined by previous researchers to identify the different wake patterns of rotating cylinders. Increasing the submergence depth in general enhances the lift generation, and this effect is more significant for the rotation with a higher spin ratio of 4 as compared to another spin ratio of 0.5. Nevertheless, the Magnus effect fails when the higher spin ratio is set at a depth of half of the cylinder diameter. As the depth is increased, the drag from the lower spin ratio decays. In contrast, the higher ratio rises significantly up to the depth of two diameters and then drops. This study clarifies the importance of the free surface in affecting the Magus effect. It is also the first time that the mode change of rotating cylinders owing to two-phase flows has been found.

I. INTRODUCTION

The flow around a rotating cylinder near the free surface has received less attention from researchers compared to the flow in a closed domain.[1–5] This type of flow is of great practical importance and has potential applications in several fields such as marine hydrodynamics and river hydraulics.[6,7] The basis of the topic is the problem of the flow around the rotating cylinder. Rotating cylinders play a crucial role in engineering and showcase a wide range of applications, such as anti-rolling systems for ships and propulsion mechanisms.[8–11] The operational principle of these cylinders is based on the Magnus effect, a phenomenon in which a rotating cylinder disrupts the flow of a fluid, causing a pressure difference that generates a lift force. This phenomenon was first described by Heinrich Gustav Magnus and has since been extensively studied in aerodynamics and hydrodynamics.[12,13]

Rotating cylinders in single-phase (SP) flows have been widely studied.[14–16] Rao *et al.*[17,18] investigated the impact of small perturbations in the incoming flow on the transition of the wake and identified a secondary kind of vortex shedding. Based on the above research, Rao *et al.*[19] proposed different modes of rotating cylindrical trails from Mode A to Mode F. Sengupta and Deepak[20] numerically studied a cylinder enforced with rotary oscillation and analyzed the flow based on the Taylor–Proudman theorem. By means of equivalent Rossby and Ekman numbers, the reason why the flow remains 2D for higher Reynolds numbers (Re) than the stationary cylinder was explained. The Reynolds number is defined as $Re = \rho U_\infty D/\mu$, where ρ is the fluid density, U_∞ denotes the inflow velocity, D is the cylinder diameter, and μ denotes the dynamic viscosity. Through experimental investigation, Chen and Rheem[21] examined the geometric shape, the Reynolds number, and the rotation speed. Their research pinpointed crucial transition zones and the dependence of hydrodynamics and vortex shedding on the rotation speed. Lin *et al.*[22] used the large-eddy simulations (LES) method to simulate three-dimensional rotating cylinders and a fully parametric modeling approach to optimize the rotation.

Two-phase flows (air and water) past stationary cylinders without any rotations have been acknowledged.[23–25] Malavasi and Guadagnini[26] investigated the interaction between the free surface and a square cylinder in a water channel, focusing on force-dominant frequencies and vortex-shedding phenomena. Results showed that asymmetric boundary conditions influence mean force coefficients and vortex shedding frequencies. Hydrodynamic forces on stationary, partially submerged cylinders were investigated through towing tests by Ren *et al.*[27] Their results demonstrated considerable changes in the hydrodynamic coefficient, and overtopping effects were found with random distributions. Zhao *et al.*[28] investigated the free surface distortion using the three-dimensional LES method for $Re = 7550$. They found that for low Froude numbers defined as $Fr = U_\infty/\sqrt{gD}$ (where g is the gravitational acceleration), the free surface has small deformation. In contrast, for high Fr, an intense distortion of the free surface appears, resulting in hydraulic jumps, long-wavelength wave generation, and water-level recovery slopes.

On the other hand, rotating cylinders within two-phase flows have only been investigated in a limited number of research endeavors. Kumar *et al.*[29] studied two counter-rotating cylinders immersed within polybutene, whose dynamic viscosity is $\mu = 12.9$ Pa s. The air entrainment patterns were explored with respect to the immersion depth and spacing between the cylinders. Panda and Rana[30] analyzed air entrainment patterns for a single rotating cylinder immersed in water, silicone oil, and polybutene. The entrainment profile, transient dynamics, and entrainment rate were examined for the different liquids. It is worth noting that in both studies,[29,30] the liquid phase is quiescent, whereas the air phase has a speed in the work of Panda and Rana.[30]

Aside from the horizontally aligned cylinders mentioned above, a vertically aligned rotating cylinder within air–water flow was tested by Abramowicz-Gerigk *et al.*,[31] where the air is quiescent but the water moves. They analyzed the flow in terms of the aspect ratio of the rotor length to diameter, rotation speed, and Re.

As evident from the literature reviewed above, none of the previous studies have delved into rotating cylinders subjected to two-phase inflow, in which both phases move at an incident speed. Nonetheless, such knowledge is highly demanded in the maritime field, for example, to develop ship anti-rolling devices. To address this concern, our research in this paper has been initialized.

This study aims to understand how a rotating cylinder reacts in a two-phase (air–liquid) flow and the resultant dynamic free-surface changes. It is to address the interrelationships among the free-surface dynamics, the wake induced by the cylinder, and the hydrodynamic forces acting on the cylinder. The factors of the spin ratio (which is defined as the ratio of the rotational line speed on the cylinder surface with respect to the inflow speed) and the immersed depth will be analyzed to figure out their effects on the alteration of the flow characteristics. Given that the inflow speed is low, both air and water will be considered incompressible. The LES integrated with the volume-of-fluid (VOF) technique will be utilized for numerical simulations.

This work is structured as follows: the numerical approach is briefly discussed in Sec. II, followed by method validation in Sec. III. The numerical simulation results are analyzed in Sec. IV. The alteration of typical modes of the flow pattern from SP flows to two-phase flows is discussed in terms of the submergence depth. The hydrodynamic forces and the downstream wake characteristics are then explored. In Sec. V, conclusions are drawn.

II. NUMERICAL METHODOLOGY

A. Governing equations

For the incompressible, viscous form of the Navier–Stokes equations, the governing equations are[32,33]

$$\frac{\partial U_i}{\partial x_i} = 0, \tag{1}$$

$$\frac{\partial U_i}{\partial t} + \frac{\partial}{\partial x_j}\left(U_i U_j + \overline{u_j' u_i'}\right) = -\frac{1}{\rho}\frac{\partial P}{\partial x_i} + \frac{1}{\rho}\frac{\partial S_{ji}}{\partial x_j} + g, \tag{2}$$

$$S_{ji} = \mu\left(\frac{\partial U_i}{\partial x_j} + \frac{\partial U_j}{\partial x_i}\right), \tag{3}$$

where U_i and U_j ($i, j = 1, 2, 3$) are the flow velocity components, x_i and x_j are the components of the coordinate vector, t is the physical time, $\overline{u_j' u_i'}$ is the Reynolds stress, P is the pressure, and S_{ji} is the average viscous stress tensor.

To accurately capture the hydrodynamic characteristics of rotating cylindrical surfaces and wake trails, complex flow separation problems have to be dealt with. The computational cost of direct numerical simulation is too high; therefore, the LES method is used in this study. Implicit filtering makes full use of the grid resolution, and the modeling cost is usually lower than that of explicit filtering. The wall-adapted local eddy-viscosity (WALE) method is used to determine the sub-grid-scale (SGS) viscosity.[34] In the LES-based numerical simulation, the bounded central-differencing scheme is used to calculate the convective flux. The governing equations for LES using the Favre filtering method are as follows:[35,36]

$$\frac{\partial \tilde{U}_i}{\partial x_i} = 0, \tag{4}$$

$$\frac{\partial \tilde{U}_i}{\partial t} + \frac{\partial \tilde{U}_i \tilde{U}_j}{\partial x_j} = -\frac{1}{\rho}\frac{\partial \tilde{P}}{\partial x_i} + \frac{\mu}{\rho}\frac{\partial^2 \tilde{U}_i}{\partial x_j \partial x_j} - \frac{\partial \tau_{ij}}{\partial x_j} + g, \tag{5}$$

$$\tau_{ij} - \frac{1}{3}\tau_{kk}\delta_{ij} = -2\nu_{sgs}\tilde{S}_{ij}, \tag{6}$$

$$\tilde{S}_{ij} = \frac{1}{2}\left(\frac{\partial U_i}{\partial x_j} + \frac{\partial U_j}{\partial x_i}\right), \tag{7}$$

$$\nu_{sgs} = (C_w \Delta)^2 \frac{\left(\mathbb{S}_{ij}^d \mathbb{S}_{ij}^d\right)^{3/2}}{\left(\tilde{S}_{ij}\tilde{S}_{ij}\right)^{5/2} + \left(\mathbb{S}_{ij}^d \mathbb{S}_{ij}^d\right)^{5/4}}, \tag{8}$$

where the symbol $\sim$ refers to the filtered quantities, τ_{ij} is the SGS stress tensor, $\tilde{S}_{ij}$ is the strain rate tensor, δ_{ij} is the Kronecker function, ν_{sgs} is the SGS eddy viscosity, Δ is the filter width, $\mathbb{S}_{ij}^d$ is the square of the traceless symmetric tensor in the velocity gradient tensor, and the C_w is the WALE constant whose value is taken as 0.544.

B. VOF method

The unsteady free surface effects are calculated using the VOF method, which is applied to track the interface of liquid and gas phases. The VOF formulation developed by Hirt and Billy[37] is based on the assumption that the two phases do not mix. In the computational cell, a variable containing the volume percent of the phase is introduced for each successive phase.[38,39] The volume fractions of all phases add up to unity in each control volume. To create a set of

equations with a comparable structure for all phases, the conservation equations for each phase are generated. The following is the continuity equation for phase q:

$$\left[\partial(\alpha_q\rho_q)/\partial t + \nabla\cdot\left(\alpha_q\rho_q\vec{U}_q\right)\right]\Big/\rho_q = S_{\alpha_q} + \sum_{p=1}^{n}\left(\dot{m}_{pq} - \dot{m}_{qp}\right), \tag{9}$$

where α_q denotes the volume fraction of phase q, ρ_q denotes the density of phase q, $\vec{U}_q$ denotes the velocity of phase q, S_{α_q} denotes the source term of the volume fraction equation, $\dot{m}_{pq}$ denotes the mass transfer from phase q to phase p, and $\dot{m}_{qp}$ denotes the mass transfer from phase p to phase q.

The main phase volume fraction fulfills the following constraint:

$$\sum_{q=1}^{n}\alpha_q = 1. \tag{10}$$

The density in each cell is given if the volume fraction of the first of these phases is tracked,

$$\rho = \alpha_1\rho_1 + (1-\alpha_1)\rho_2, \tag{11}$$

where subscripts 1 and 2 represent the liquid and gas phases of the two-phase flow objective, respectively.

Other parameters, involving viscosity, are estimated in a similar manner. The momentum equation is solved throughout the whole computational domain, and the resulting velocity field $\vec{U}$ is distributed across the phases as follows:

$$\partial(\rho\vec{U})/\partial t + \nabla\cdot(\rho|\vec{U}\vec{U}) = -\nabla P + \nabla\cdot\left[\mu\left(\nabla\vec{U} + \nabla\vec{U}^{T}\right)\right] + \rho\vec{g} + \vec{f}, \tag{12}$$

where $\vec{g}$ is the acceleration of gravity and $\vec{f}$ is the source of the interface force.

The key parameters of the simulated cases are detailed in Nomenclature.

C. Numerical settings

Figure 1 illustrates a sectional view of the computational domain and boundary conditions for the problem investigated in this paper. The computational domain is three-dimensional and has a spanwise length of $L = 3\,D$. The entrance boundary is set at the velocity inlet and is $10\,D$ from the center of the cylinder. The outlet boundary is configured as a pressure outlet and is $75\,D$ from the cylinder's center. VOF wave damping is required to limit wave reflection, with the damping length stated to be one-time the cylinder diameter. The cylinder, defined as a no-slip wall surface, rotates in a clockwise direction. The dimensionless rotational speed of the cylinder, i.e., the spin ratio, is defined as $\alpha = \omega D/2U_\infty$, where ω is the rotational speed. All other far-field boundaries are set to the plane of symmetry. The liquid depth is $20\,D + H$, where H is the depth of submergence. The depth ratio (H/D) is changed from 0.5 to 2.0 in this work. The top boundary is $10\,D$ above the initial free surface. Gravity is counted in both phases. In the LES, the time step is determined by rotating the cylinder with 1° per time step. The data acquisition time is 100 periods of tU_∞/D.

D. Computational meshes

The mesh generation process is critical to the accuracy and dependability of the findings. The mesh size and distribution are determined based on the flow conditions, cylinder geometry, and simulation requirements. An overset mesh approach is used to make the cylinder rotate. In the overset region, the structured grid is fine around the cylinder to capture the complex flow patterns and gradients, gradually transitioning to a coarser grid away from the cylinder. In the background region, the free surface and flow areas are locally refined using an unstructured (trimmed) mesh. There is an overlap zone between these two regions, which have different cells. The management of boundary conditions gets more complicated because of the use of the overset mesh. Interpolation and transferring of physical variables across distinct mesh layers in the overlap zone are necessary to maintain physical conservation and numerical stability.

The grid of the computational domain is shown in Fig. 2. The vertical length of the free surface refinement region is $1.28\,D$, with a minimum and maximum vertical cell size of $0.04\,D$ and $0.08\,D$, respectively, requiring 24 cells along the vertical direction. The rotational mesh has a diameter of $5\,D$. The first layer cell height is $1.4\times10^{-4}\,D$, and the maximum cell size within the rotational mesh is

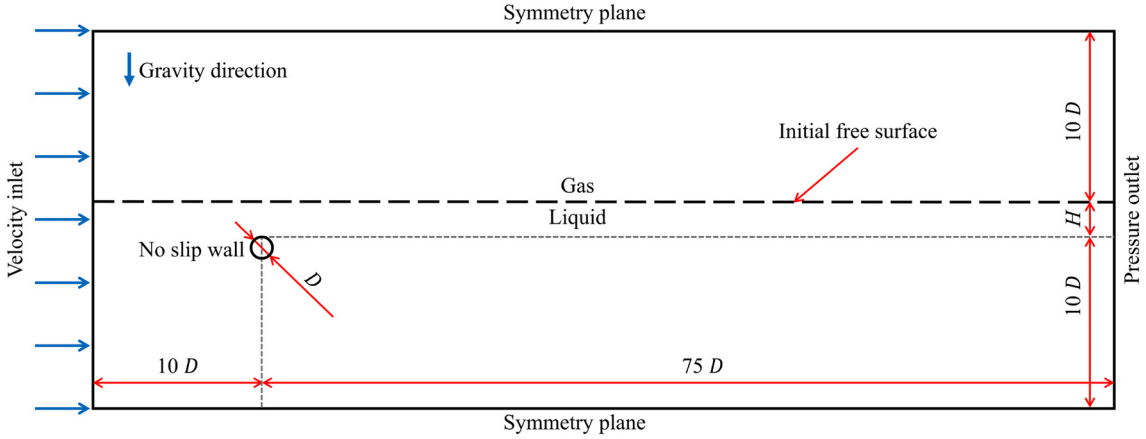

FIG. 1. The computational domain and boundary conditions, where H denotes the submergence depth, which is the vertical distance from the initial free surface to the cylinder surface.

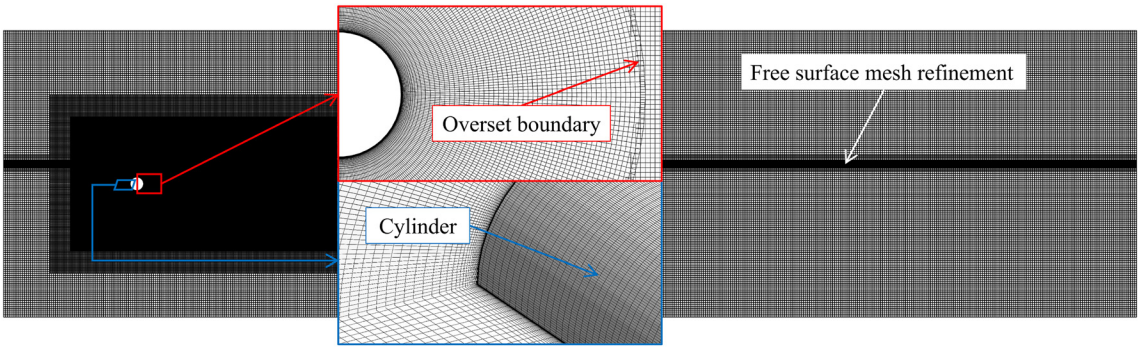

FIG. 2. The computational mesh at different positions.

0.04 D. According to the current mesh parameters, the dimensionless wall distance y+ at the cylinder surface is less than 1. This guarantees that the mesh resolution for the boundary layer is maintained. The spanwise cell size is uniform, with a maximum of 0.04 D near the cylinder surface. The background mesh has three refinement levels, with the finest level having the same cell size as the rotational domain. The largest cell size is 0.16 D near the boundaries.

III. NUMERICAL VERIFICATION

Because there are no relevant experimental or numerical data in the literature that have been conducted for the same research problem as our present work, the numerical approach in this study is validated first for rotating cylinders in SP flow at varied Re and the spin ratio α. After that, the numerical approach is validated for a stationary cylinder in a two-phase flow interacting with a free surface. Finally, the mesh quality is examined for the cylinder rotating within the two-phase flow.

Table I compares and verifies the numerical simulation results for rotating cylinders in the SP flow at different Re and α. The lift coefficient $(C_l = F_l/(0.5\rho_1 LDU_\infty^2))$ and the Strouhal number $(S_t = fD/U_\infty)$ are compared, where F_l is the lift force of the cylinder and f is the frequency of vortex shedding, determined by applying a fast Fourier transform to the time-history curve of F_l. The comparison shows that the deviations in the mean values of C_l and S_t under different operating conditions are smaller than 3%.

The instantaneous flow fields near the cylinder at the different spin ratios are compared to the results of Mittal and Kumar[40] in Fig. 3. As can be seen, the flow separation locations in the present simulations are consistent with the previous study.

Table II compares the present results to those of Colagrossi *et al.*[42] for stationary cylinders at various Fr. The S_t, C_l, and drag coefficients $(C_d = F_d/(0.5\rho_1 LDU_\infty^2))$ are compared, where F_d is the drag force of the cylinder. When considering SP flow, the amplitude of C_l is contrasted since the mean C_l is zero. The results show that the C_l, C_d, and S_t deviations are all within 4% compared to the simulations of Colagrossi *et al.*,[42] and the morphology of the trailing vorticity remains in good agreement across Fr.

Figure 4 depicts the vorticity fields under the free surface for various Fr in comparison with the results of Colagrossi *et al.*[42] The topology of the vortex structures computed in the present work is nearly the same as that of the previous study.

Mesh generation is an iterative process that strives to achieve a balance between resolution and computational cost. When $Re = 250$, $Fr = 0.47$, $\alpha = 0.5$, and $H/D = 1$, the grid convergence is analyzed, and the results are shown in Table III. Three sets of meshes with total cell numbers of 14.6, 10.3, and 7.5×10^6 are used for the validation. The grid convergence index (GCI) approach is adopted in this work to assess the discretization error. The GCI gives a confidence level for predicting the error range with a safety factor of 1.25 and is reported as a percentage of error, which

TABLE I. Numerical simulation results for rotating cylinders in single-phase flow.

	Re	α	C_l	Error of C_l (%)	S_t	Error of S_t (%)
Mittal and Kumar[40]	200	1	2.47	⋯	0.191	⋯
This work	200	1	2.51	1.51	0.187	−2.43
Mittal and Kumar[40]	200	2	5.68	⋯	0.183	—
This work	200	2	5.80	1.99	0.179	−2.60
Mittal and Kumar[40]	200	3	10.33	⋯	⋯	⋯
This work	200	3	10.06	−2.64	⋯	⋯
Mittal and Kumar[40]	200	4	17.67	⋯	⋯	⋯
This work	200	4	17.19	−2.71	⋯	⋯
Munir *et al.*[41]	250	4	15.54	⋯	⋯	⋯
This work	250	4	15.08	−2.96	⋯	⋯

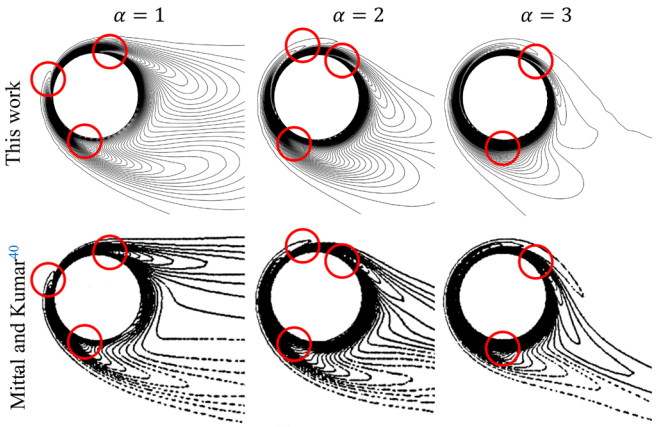

FIG. 3. The instantaneous vorticity field for the rotating cylinder in single-phase flow ($Re = 200$) at the spin ratios of 1, 2, and 3. The flow separation locations are labeled with red circles.

corresponds to a 95% confidence interval.[43,44] In accordance with the ITTC's 2017 recommendation, the grid refinement ratio was chosen as 2.[45] The results show that the GCIs for both C_l and C_d are less than 2%, which is acceptable. Ultimately, the mesh of about 14×10^6 grid cells was used in the follow-up study to ensure the accuracy of the results.

TABLE III. The results of the grid convergence.

Mesh	Total number of grid cells ($\times 10^6$)	C_l	GCI of C_l (%)	C_d	GCI of C_d (%)
Fine	14.6	1.086	0.57	1.804	0.85
Medium	10.3	1.094	1.49	1.827	2.44
Coarse	7.5	1.115	···	1.835	···

IV. RESULTS AND DISCUSSION

There are multiple modes of wake induced by rotating cylinders in SP flows with respect to Re and the spin ratio α.[19,46–48] When $Re = 250$ and $Fr = 0.47$, two typical wake modes, such as Modes A and E, occur at $\alpha = 0.5$ and 4.0, respectively, according to Rao *et al.*[19] The previous studies demonstrated that in SP flows, Mode A exhibits classical Bénard–von Kármán (BvK) vortex shedding. On the contrary, in mode E, BvK vortex shedding is suppressed. It is therefore interesting to

TABLE II. Numerical simulation results for stationary cylinders at $Re = 180$ at various Fr.

	Fr	H/D	C_l	Error of C_l (%)	C_d	Error of C_d (%)	S_t	Error of S_t (%)
Colagrossi *et al.*[42]	0.30	0.4	−0.41	···	1.66	···	0.192	···
This work	0.30	0.4	−0.42	2.74	1.69	1.52	0.199	3.66
Colagrossi *et al.*[42]	0.55	0.4	−0.46	···	1.48	···	0.217	···
This work	0.55	0.4	−0.48	3.58	1.42	−3.90	0.221	1.82
Colagrossi *et al.*[42]	0.34	SP	0.61	···	1.29	···	0.193	···
This work	0.34	SP	0.59	−3.17	1.33	−3.06	0.191	−1.12

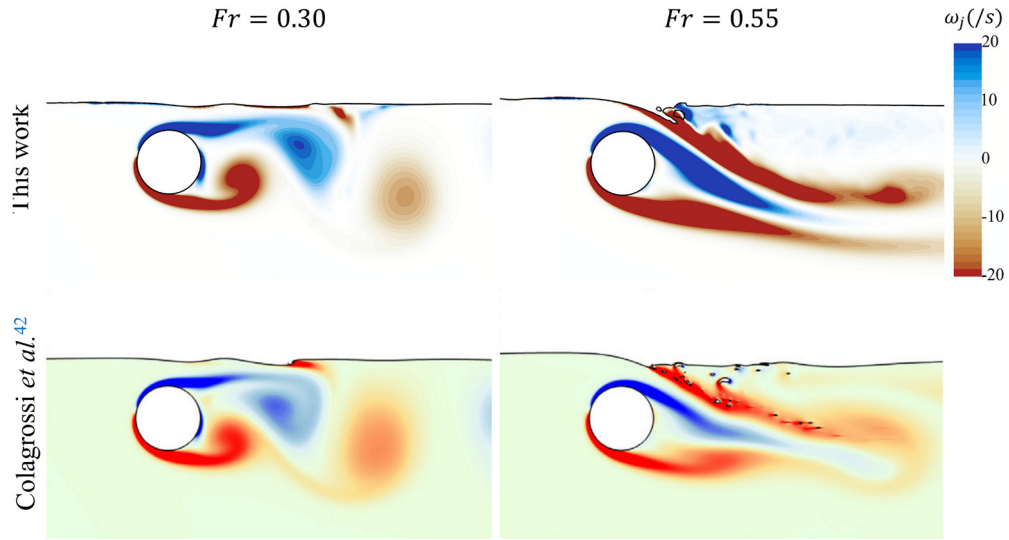

FIG. 4. Contours of the spanwise vorticity component ω_j for the stationary cylinder in two-phase flow ($Re = 180$) at $Fr = 0.3$ and 0.55.

understand how these modes at the same Re, Fr, and α are altered because of the presence of the free surface in the two-phase flow.

A. Mode-A-related vortex development and interaction with the free surface

Mode A in SP flows exists at the spin ratio of $\alpha = 0.5$. Correspondingly, in the two-phase flow, contours of the dimensionless streamwise velocity (U_x/U_∞) at the submergence ratios of $H/D = 0.5$, 1.0, 1.5, and 2.0 are shown in Fig. 5, where U_x denotes the streamwise velocity. As the cylinder rotates clockwise, it increases the flow velocity between the upper surface of the cylinder and the free surface. According to the Magnus effect in the SP flow, the wake is deflected toward the downward side. This phenomenon is also observed at all submerged depths of the two-phase flow.

Rao *et al.*[19] reported that classical BvK vortex shedding exists in Mode A of the SP flow. However, as can be seen for the two-phase flow in Fig. 5, the shedding disappears at the small submergence ratios of $H/D = 0.5$ and 1.0. The reason is that the free surface between the air and water dynamically interacts with the rotating cylinder, in particular the velocity field on the upper side of the cylinder. The alteration suppresses the periodic asymmetry vortex detachment. As a result, the wake is streaked without the formation of a vortex street. Meanwhile, a backflow zone is observed in terms of the negative streamwise velocity. The length of the zone decreases as the submergence ratio is increased since the interaction between the free surface and the cylinder is weakened. When the submergence ratio is increased to 1.5 and 2.0, the flow patterns become similar to mode A of the SP flow.

Figure 6 illustrates the distribution of the spanwise vorticity component ω_j for the different H/D at $\alpha = 0.5$. It can be observed that the presence of a free surface greatly inhibits the formation of vortex streets close to the surface. A distinct BvK vortex street is formed in the wake at $H/D \geq 1.5$, similar to the results in the SP flow, corresponding to mode A. However, the vortex street at $H/D \leq 1.0$ is suppressed, and the tail vortex pattern shifts to mode E of the SP flow that was described by Rao *et al.*[19] Vortices formed because of the gas being entrained in the liquid can be observed at the free surface directly above the cylinder, approximating the flow field of the near-free surface stationary cylinder with $Fr = 0.55$ in Fig. 4. It can be seen that the properties of two-phase flows are usually more complex than those of SP flows because the interaction between different phases affects the overall behavior of the fluid. For example, the relative velocities and

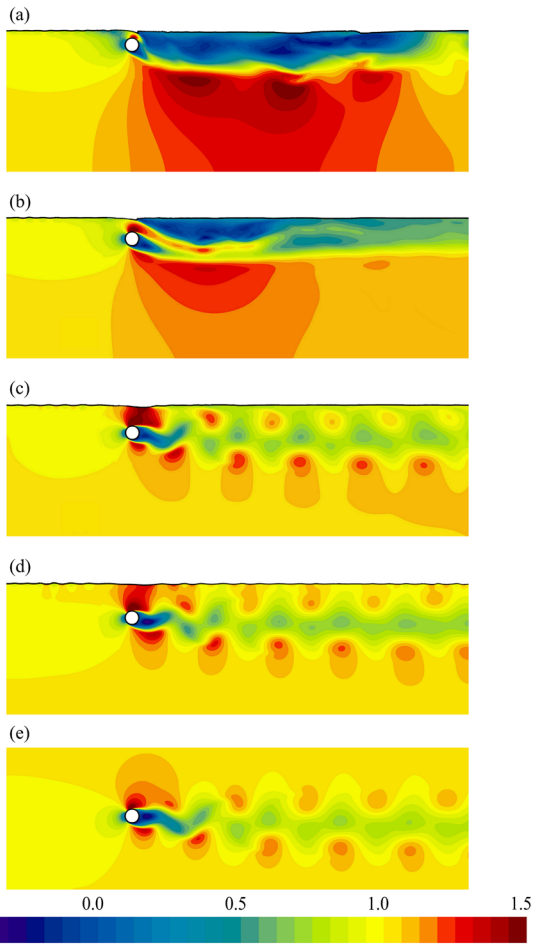

FIG. 5. The distributions of the dimensionless streamwise velocity for the spin ratio of $\alpha = 0.5$ at the different submergence ratios: (a) $H/D = 0.5$, (b) $H/D = 1.0$, (c) $H/D = 1.5$, (d) $H/D = 2.0$, and (e) SP.

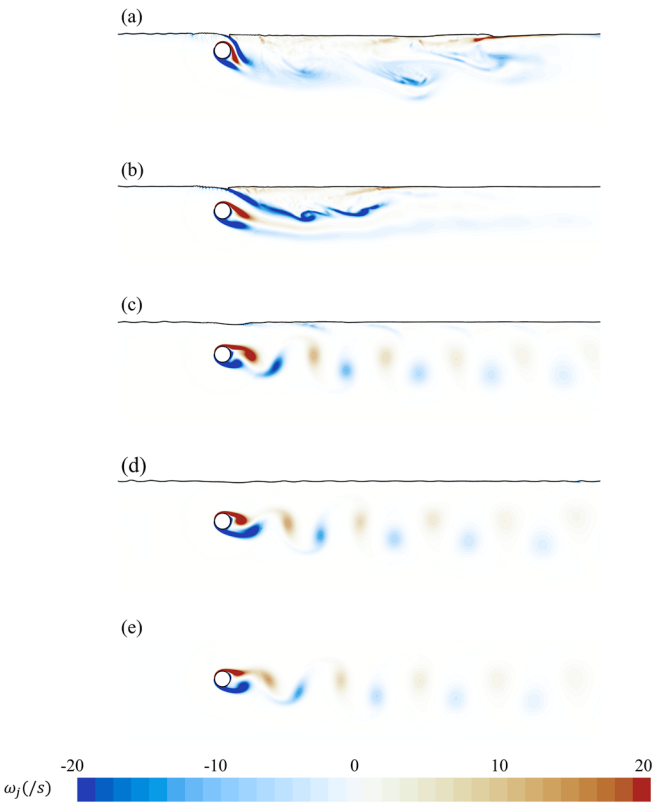

FIG. 6. Contours of the spanwise vorticity component ω_j for $\alpha = 0.5$ at the different submergence depths: (a) $H/D = 0.5$, (b) $H/D = 1.0$, (c) $H/D = 1.5$, (d) $H/D = 2.0$, and (e) SP.

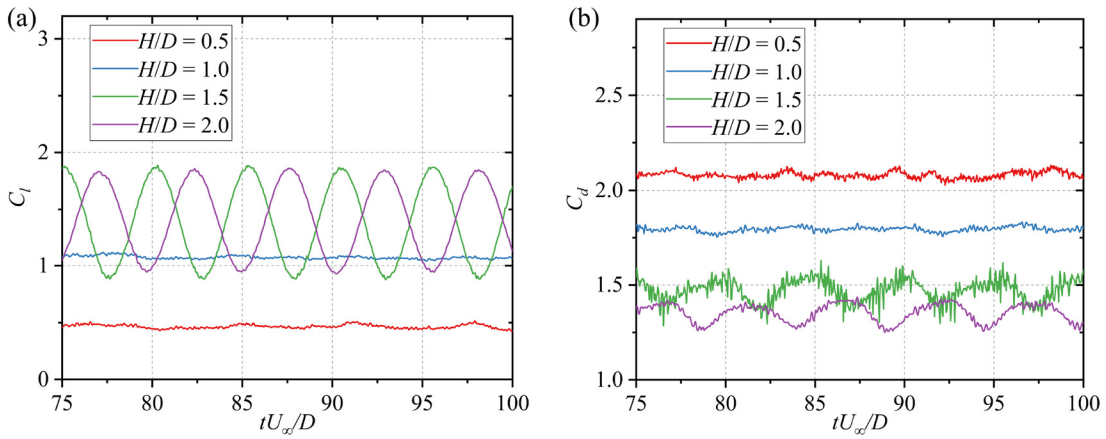

FIG. 7. The time history of (a) the lift coefficient and (b) the drag coefficient at the different submergence depths when the spin ratio of the rotating cylinder is $\alpha = 0.5$.

different densities between the gas and the liquid can lead to flow phenomena such as bubbling and flow separation. In addition, the transfer and conversion processes in two-phase flows are different from those in SP flows.

The time histories of C_l and C_d for $\alpha = 0.5$ at $H/D = 0.5$, 1.0, 1.5, and 2.0 are shown in Fig. 7. Both coefficients show small fluctuations for $H/D = 0.5$ and 1.0. These effects are associated with the interaction between the free surface and the vortices induced downstream of the cylinder. It is evident that the dynamics of the free surface affect the hydrodynamic forces when the cylinder is positioned closely to the free surface. In contrast, there are large periodic oscillations for the other higher submergence ratios of $H/D = 1.5$ and 2.0. This effect is explained with reference to Figs. 5 and 6. Mode A with the BvK vortex street plays a role in generating the large oscillatory forces.

B. Mode-E-related vortex development and interaction with the free surface

Figure 8 presents the distribution of the dimensionless streamwise velocity for $\alpha = 4.0$ at the different H/D. Coherent vortices are not observed in these cases, in contrast to the cases of $\alpha = 0.5$ at $H/D = 1.5$ and 2.0, where the BvK vortex shedding related to mode A is found. According to the results for SP flows,[19,46–48] the flow pattern at $\alpha = 4.0$ with current $Re = 250$ and $Fr = 0.47$ is categorized as mode E, in which induced vortices embrace the rotating cylinder without the formation of a vortex street. Instead, at submergence ratios of 0.5 and 1.0, a zone of negative streamwise velocity commences upstream of the cylinder and is blended with the wake downstream of the cylinder. When the submergence ratio is further increased, the negative velocity zone moves in the downstream direction and is separated from the cylinder.

The contours of the spanwise vorticity component ω_j for $\alpha = 4.0$ at the different H/D are shown in Fig. 9. Turbulent vortices downstream of the cylinder increase substantially as compared to the cases of $\alpha = 0.5$. Moreover, vorticity magnitudes in all two-phase cases are overall much larger than those in the SP flow. This indicates that the free surface imposes a significant impact. In the cases of $H/D = 0.5$,

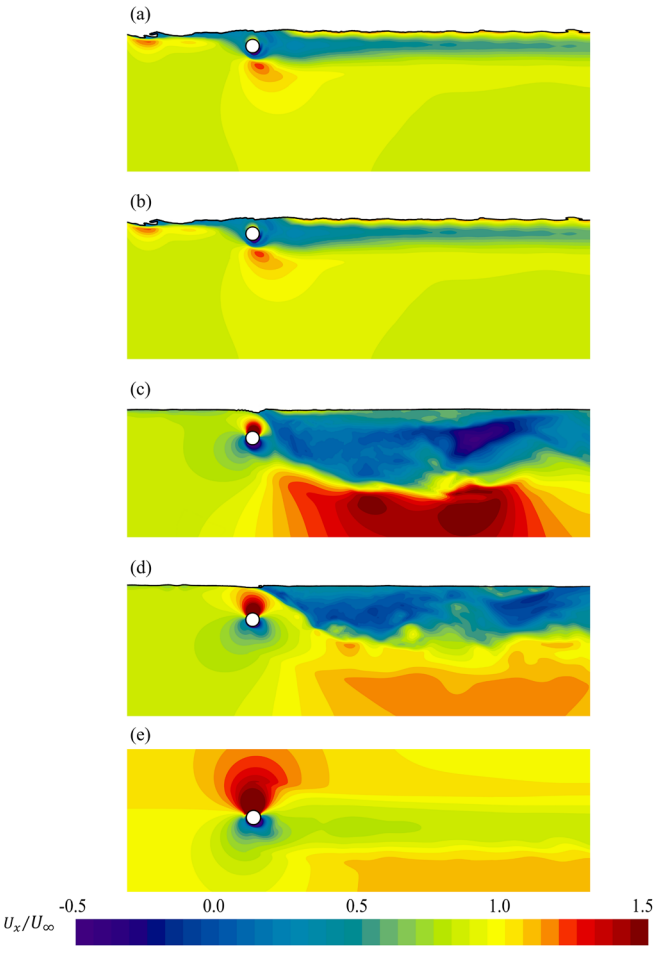

FIG. 8. The distributions of the dimensionless streamwise velocity for the spin ratio of $\alpha = 4.0$ at the different submergence ratios: (a) $H/D = 0.5$, (b) $H/D = 1.0$, (c) $H/D = 1.5$, (d) $H/D = 2.0$, and (e) SP.

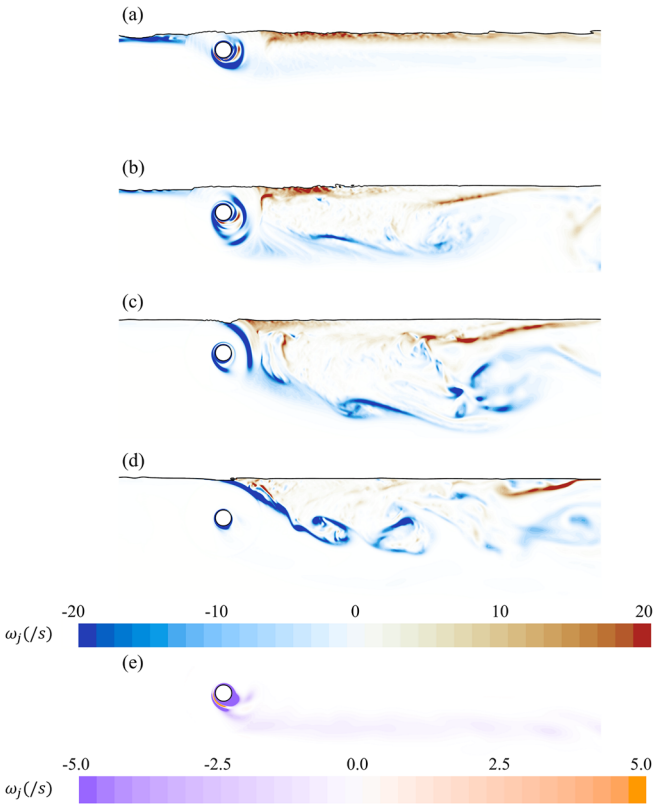

FIG. 9. Contours of the spanwise vorticity component ω_j for $\alpha = 4.0$ at the different submergence depths: (a) $H/D = 0.5$, (b) $H/D = 1.0$, (c) $H/D = 1.5$, (d) $H/D = 2.0$, and (e) SP.

1.0, and 1.5, where the free surface is closer to the cylinder, intensive vortices appear near the cylinder and are driven to follow the cylinder rotation. This flow pattern of the two-phase flows is more similar to mode F′ of the SP flow that was defined by Rao *et al.*[19] However, when $H/D = 2.0$, the flow pattern becomes Mode E like the SP flow at the same spin ratio, indicating that the effect of the free surface becomes weakened. In addition, the wake at $H/D = 0.5$ is nearly parallel to the free surface, while it is known that the wake in the SP flow is swept downward [see Fig. 9(e)]. This change in the swept direction is also associated with the close distance between the free surface and the cylinder.

In Fig. 10, the lift and drag coefficients in the cases with the larger spin ratio of $\alpha = 4$ at the different H/D are displayed. A large number of short-period fluctuations are observed in both lift and drag in all cases. Apart from that, the cases with low submergence depth ratios of 0.5 and 1.0 exhibit long-period fluctuations in the force coefficients, whereas such long-period fluctuations disappear in the higher depth cases, although there are ultra-long period ones existing. As can be seen in Fig. 9, turbulent vortices account for the intensive perturbations in the forces. It is worth noting that the behavior at the ratio of 2.0 is rather different from the other cases regarding the magnitude of C_d, which is smaller than the 1.5 case and does not follow the trend that the drag increases with the submergence depth. This significant drag reduction results from the effect signified in Fig. 8; that is, the backflow zone with the negative velocity is separated from the cylinder's near field when $H/D = 2.0$.

C. Hydrodynamic forces in dependence of the submergence depth

The curves of the time-averaged lift and drag coefficients C_l and C_d with the submergence ratio H/D for different modes are presented in Fig. 11. As the submergence ratio increases, the case with the low spin ratio of $\alpha = 0.5$ shows slightly increased C_l but decreased C_d, and the change levels of these coefficients tend to become smaller. This suggests that the effects of the free surface on the hydrodynamic forces turn out to be insignificant for a large submergence depth. On the other hand, for the high spin ratio of $\alpha = 4$, the lift and drag coefficients are significantly affected by the submergence ratio.

Although it has been known that in SP flows the rotating cylinder produces a positive lift force,[41] there is a negative lift coefficient of -0.982 observed in the present case of $\alpha = 4$ with the submergence ratio of $H/D = 0.5$, which is closest to the initial free surface. It means that the Magnus effect fails in this situation. The lift rises substantially

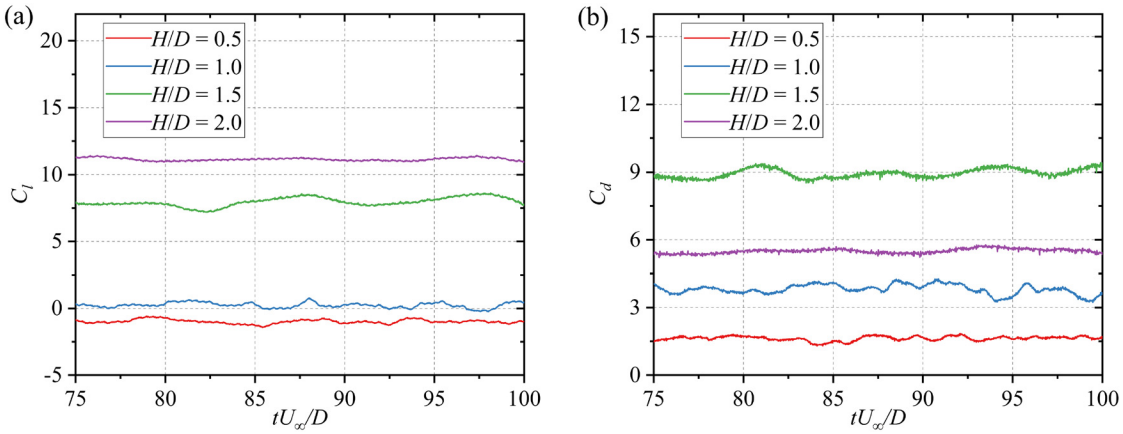

FIG. 10. The time history of (a) the lift coefficient and (b) the drag coefficient at the different submergence depths when the spin ratio of the rotating cylinder is $\alpha = 4.0$.

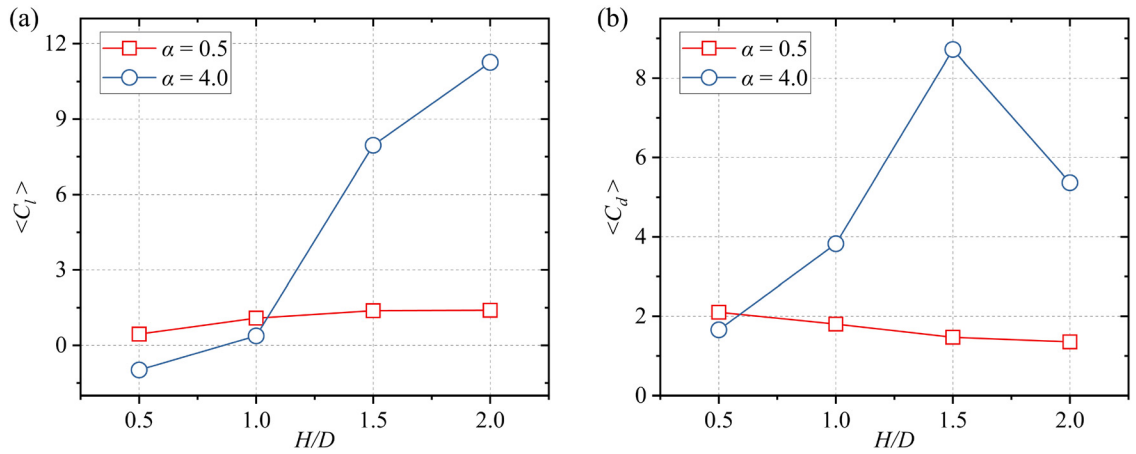

FIG. 11. The time-averaged values of (a) the lift coefficient and (b) the drag coefficient as a function of the submergence ratio at the spin ratios of $\alpha = 0.5$ and 4.

with respect to the submergence ratio. As reported by Munir *et al.*,[41] the lift coefficient in the SP flow is 15.54. The SP flow can be regarded as an extreme situation of the two-phase flow, where H/D is infinite. Therefore, the lift will increase up to the value of the SP flow once the submergence depth is large enough to neglect the influence of the free surface between the air and water. The drag for $\alpha = 4$ increases up to $H/D = 0.5$, but it drops when further increasing the submergence ratio. According to the study in Ref. 41, C_d is 0.03 in the SP flow that has the same *Re* and *Fr* at $\alpha = 4$ as the present two-phase flows. Given that the SP flow corresponds to infinite H/D, the extreme value that the rotating cylinder with the same spin ratio in two-phase flows can reach is 0.03.

Figure 12 analyzes the distribution of the transient pressure coefficients (C_p) on the cylindrical surface at various α and H/D values. The transverse coordinates are the circumference angles (θ) of monitoring points on the surface of the cylinder, with 0° associated with the leftmost point of the cylinder and the degree increasing counterclockwise. From Fig. 12(a), the absolute value of the minimum C_p gradually increases with respect to H/D, and the corresponding value of θ also increases, i.e., shifting toward the downstream direction. Since the asymmetry in pressure distribution between the upper and lower surfaces of the cylinder increases, a rise of $\langle C_l \rangle$ is observed in Fig. 11. The minimum value of C_p is near $\theta = 275°$ for $\alpha = 0.5$ at H/D of 1.5 and 2.0, and close to 225° and 248° for $\alpha = 4.0$ at H/D of 1.5 and 2.0. The results indicate the direction of the wake deflection, as illustrated in Figs. 6 and 9.

As shown in Fig. 12(b) for $\alpha = 4.0$, C_p in the case of $H/D = 0.5$ reaches its lowest point near $\theta = 120°$. This phenomenon is quite different from those under the other working conditions, leading to the negative value of $\langle C_l \rangle$ [see Fig. 11(a)]. When $H/D \geq 1.5$, the pressure difference due to the asymmetry distribution on the upper and lower surfaces of the cylinder increases significantly. Consequently, a noticeable growth of $\langle C_l \rangle$ is seen in Fig. 11(a). Moreover, as found in Fig. 11(b), the time-averaged $\langle C_d \rangle$ at $\alpha = 4.0$ reaches the largest value at the submergence ratio of 1.5. The abnormal phenomenon implies the transition of vortices from modes F′ to E in the wake, which is caused by the interaction with the free surface.

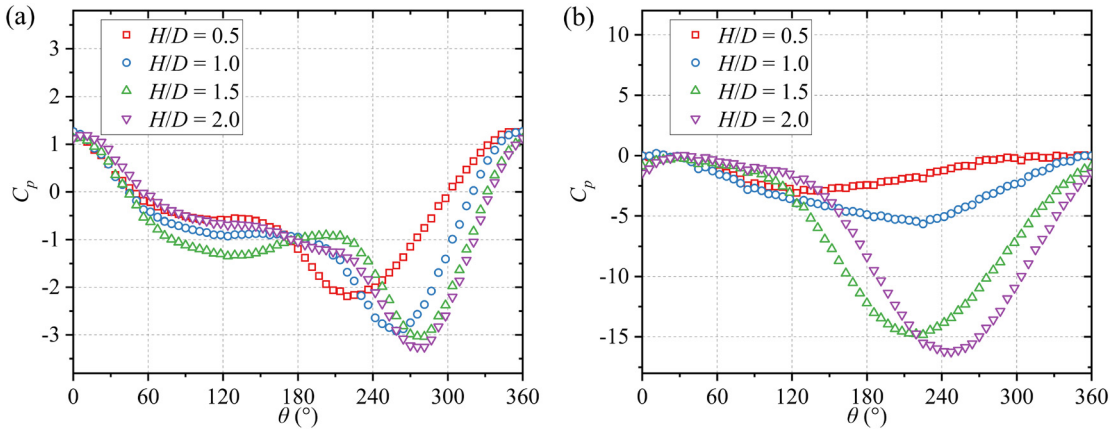

FIG. 12. The pressure coefficients on the cylindrical surfaces at different submergence depths for (a) $\alpha = 0.5$ and (b) $\alpha = 4.0$.

D. Induced free-surface waves downstream of the cylinder

Figure 13 depicts the boundary line of the free surface in the far downstream region ($50 \leq x/D \leq 75$), which is defined as the vertical displacement of the free surface with respect to its initial position. For all cases over the two spin ratios, fluctuations of long wave lengths are observed at relatively low submergence ratios, smaller than 2.0. However, this type of fluctuation disappears at the highest submergence ratio for both low and high cylinder spin ratios. It signifies that free surface waves driven by the cylinder's rotation become nearly negligible. In other words, the interaction between the free surface and the wake induced by the cylinder will be minor if the submergence depth is larger than $2D$.

As can also be seen in Fig. 13, for the low spin ratio, the submergence ratios from 0.5 to 1.5 account for overall larger fluctuations than the ratio of 2.0. This implies significant interactions between the free surface and the wake. Similarly, the high spin ratio results in large fluctuations for all three smaller submergence ratios, including $H/D = 0.5$. However, the average surface level is lifted at submergence ratios of 0.5 and 1.0. This effect is only seen with the high spin ratio of the cylinder. The cause is that increasing the spin ratio enhances the interaction between the free surface and the cylinder wake.

The normalized power spectral densities (PSDs) of the vertical displacements of free-surface waves monitored right above the cylinder are shown in Fig. 14. The dimensionless frequency is defined as the Strouhal number $St = fD/U_\infty$. The PSD normalization is made as $\overline{PSD} = PSD \cdot f_0/D^2$, where f_0 is the characteristic frequency of the wake caused by the rotating cylinder. For all cases with the various spin ratios and submergence depths, the most predominant peak occurs at f_0. Thus, the free-surface variations are dependent on the cylinder rotation.

V. CONCLUSIONS

In this paper, the hydrodynamics of a rotating cylinder in the presence of the free surface within an air–liquid flow, as well as the characteristics of the generated free-surface waves, are investigated numerically. The impacts of the spin ratio and submergence depth are analyzed in connection with the characteristic flow patterns in SP flows, especially modes A, E, and F′. The main findings of this study are summarized as follows:

1. As the cylinder rotates with a spin ratio of $\alpha = 0.5$ in the two-phase flow, the submergence depth affects the change of the flow modes. At $H/D = 0.5$ and 1.0, the free surface alters the flow pattern from mode A in SP flow to mode E. At larger submergence ratios of 1.5 and 2.0, mode A persists in two-phase flows like SP flow. Mode A causes periodic fluctuations in lift and drag forces on the cylinder, while mode E results in small fluctuations in the forces.
2. Once the spin ratio of the cylinder is increased to 4.0, the flow pattern at submergence ratios less than 2.0 is altered to mode F′, while at 2.0 it becomes back to mode E like the SP flow included by the same cylinder rotation. In addition, at $\alpha = 0.5$, the wake

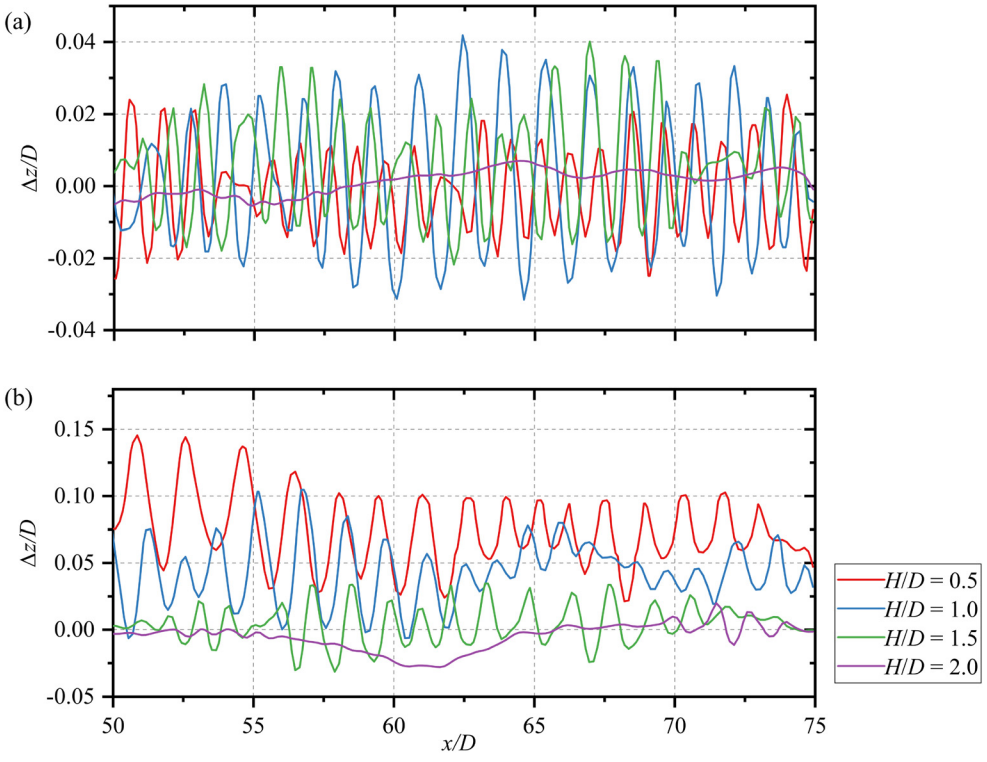

FIG. 13. Transient vertical displacements of the free surface in reference to its initial position at the different submergence ratios for the spin ratios: (a) $\alpha = 0.5$ and (b) $\alpha = 4.0$.

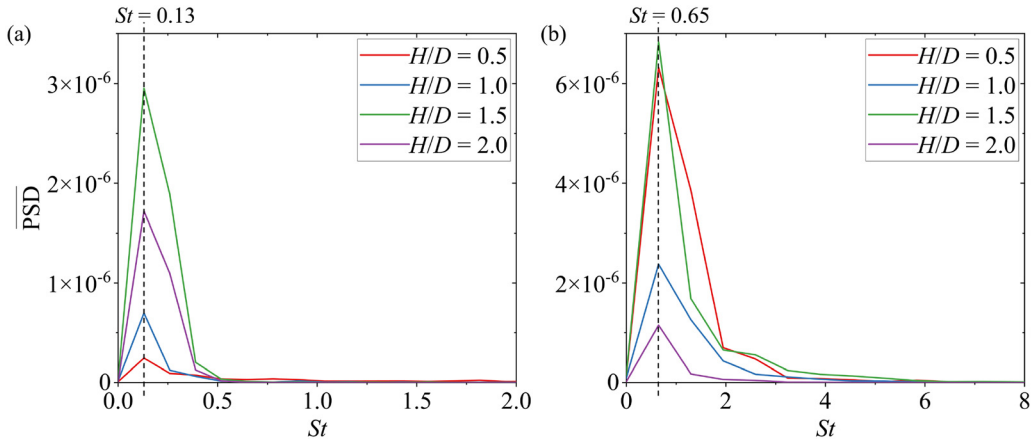

FIG. 14. The normalized PSDs of the vertical displacements of free-surface waves for the spin ratios are (a) $\alpha = 0.5$ and (b) $\alpha = 4.0$.

deflection is suppressed because of the significant interaction between the free surface and the cylinder. The lift and drag forces in mode F′ include relatively larger-amplitude and longer-period fluctuations in addition to small fluctuations. In contrast, only small fluctuations are observable in mode E.

3. An increase in the submergence depth gives rise to an increased lift force for both spin ratios of the cylinder. The higher spin ratio introduces a much more significant increase in rate. However, an abnormal case is at the submergence ratio of 0.5, where the lift force is negative. It suggests that the Magus effect fails due to the presence of the free surface.
4. The increased submergence depth results in a drag reduction for the lower spin ratio, but an increase for the higher spin ratio, except for the largest submergence depth. Regarding the higher spin ratio, the flow pattern is changed from modes F′ to E with respect to the increased submergence depth. Therefore, the drag drop is associated with the mode change.
5. The primary wave frequency is close to the characteristic Strouhal number of the rotating cylinder. However, waves are insignificant for the largest submergence ratio of 2.0, meaning that the wake induced by the cylinder has a limited effect on free surface development. Moreover, the free surface over the cylinder varies at a dimensionless frequency that is equal to the characteristic Strouhal number of the cylinder. It indicates that the cylinder rotation dominates the dynamics of the free surface.

In future research, it will be interesting to change the rotational direction of the cylinder and observe its effect on free surface waves and hydrodynamic forces. If the cylinder is rotated counterclockwise, the lift force may point downward instead of upward as it does in clockwise rotation. The relationship between the spin ratio and the submergence depth should also be changed. A consequence would be different mechanisms in the formation and propagation of free surface waves. In addition, the interaction of horizontally or vertically aligned cylinders in two-phase flow can be studied. By gaining a deeper understanding of how these factors interact and affect free surfaces, the phenomenon can be better understood and provided more basis for practical applications.

ACKNOWLEDGMENTS

The computations and data handling were enabled by resources provided by the Swedish National Infrastructure for Computing (SNIC) at the National Supercomputer Centre (NSC) at Linköping University, partially funded by the Swedish Research Council through Grant Agreement No. 2018-05973. The work was supported by the China Scholarship Council (Grant No. 202106680052), the Strategic Research Project on Hydro- and Aerodynamic Initiative financed by the Chalmers Foundation, and the innovation project by Lighthouse (Grant No. FS24_2022).

AUTHOR DECLARATIONS

Conflict of Interest

The authors have no conflicts to disclose.

Author Contributions

Jianfeng Lin: Investigation (equal); Software (equal); Validation (equal); Visualization (equal); Writing – original draft (equal); Writing – review & editing (equal). **Hua-Dong Yao:** Conceptualization (equal); Methodology (equal); Resources (equal); Supervision (equal); Validation (equal); Writing – original draft (equal); Writing – review & editing (equal).

DATA AVAILABILITY

The data that support the findings of this study are available within the article.

NOMENCLATURE

D	Diameter of the cylinder
g	Gravitational acceleration
H	Distance from the cylinder to the free surface
L	Spanwise length of the cylinder
Re	Reynolds number
U_∞	Inflow velocity

α Spin ratio
μ Dynamic viscosity of the fluid
ρ Fluid density

REFERENCES

[1]R. Subburaj, P. Khandelwal, and S. Vengadesan, "Numerical study of flow past an elliptic cylinder near a free surface," Phys. Fluids **30**(10), 103603 (2018).
[2]F. Zafar and M. M. Alam, "Flow structure around and heat transfer from cylinders modified from square to circular," Phys. Fluids **31**(8), 083604 (2019).
[3]S. K. Panda, B. K. Rana, and P. Kumar, "Competition of roller rotation and horizontal crossflow to control the free surface cusp-induced air entrainment," Phys. Fluids **33**(11), 112114 (2021).
[4]B. F. Feshalami, S. He, F. Scarano, L. Gan, and C. Morton, "A review of experiments on stationary bluff body wakes," Phys. Fluids **34**(1), 011301 (2022).
[5]T. Erfan, M. Zhao, and H. Wu, "The enhancement of flow induced vibration of a circular cylinder using a rotating control rod," Phys. Fluids **35**(4), 043607 (2023).
[6]D. Ozturk, "Performance of a Magnus effect-based cylindrical roll stabilizer on a full-scale Motor-yacht," Ocean Eng. **218**(15), 108247 (2020).
[7]H. Akyildiz and Ö. İ. Aydin, "On the Magnus rotating roll stabilizer; numerical and experimental studies," GİDB Dergi **22**, 37–68 (2022), see https://dergipark.org.tr/en/pub/gidb/issue/73057/1164674#article_cite.
[8]T. Craft, N. Johnson, and B. Launder, "Back to the future? A re-examination of the aerodynamics of Flettner-Thom rotors for maritime propulsion," Flow, Turbul. Combust. **92**, 413–427 (2014).
[9]J. Lin, Y. Han, Y. Su, and Z. Zhang, "Magnus antirolling system for ships at zero speed," IEEE Trans. Transp. Electrif. **7**(4), 3062–3069 (2021).
[10]J. Lin, Y. Han, C. Guo, Y. Su, and R. Zhong, "Intelligent ship anti-rolling control system based on a deep deterministic policy gradient algorithm and the Magnus effect," Phys. Fluids **34**(5), 057102 (2022).
[11]V. Vigna and M. Figari, "Wind-assisted ship propulsion: Matching Flettner rotors with diesel engines and controllable pitch propellers," J. Mar. Sci. Eng. **11**(5), 1072 (2023).
[12]W. M. Swanson, "The Magnus effect: A summary of investigations to date," J. Basic Eng. **83**, 461–470 (1961).
[13]J. Seifert, "A review of the Magnus effect in aeronautics," Prog. Aerosp. Sci. **55**, 17–45 (2012).
[14]S. Kumar, B. Gonzalez, and O. Probst, "Flow past two rotating cylinders," Phys. Fluids **23**(1), 014102 (2011).
[15]A. R. Teymourtash and S. E. Salimipour, "Compressibility effects on the flow past a rotating cylinder," Phys. Fluids **29**(1), 016101 (2017).
[16]P. Sundaram, T. K. Sengupta, A. Sengupta, and V. K. Suman, "Multiscale instabilities of Magnus–Robins effect for compressible flow past rotating cylinder," Phys. Fluids **33**(3), 034129 (2021).
[17]A. Rao, J. S. Leontini, M. C. Thompson, and K. Hourigan, "Three-dimensionality in the wake of a rapidly rotating cylinder in uniform flow," J. Fluid Mech. **730**, 379–391 (2013).
[18]A. Rao, A. Radi, J. S. Leontini, M. C. Thompson, J. Sheridan, and K. Hourigan, "The influence of a small upstream wire on transition in a rotating cylinder wake," J. Fluid Mech. **769**, R2 (2015).
[19]A. Rao, A. Radi, J. S. Leontini, M. C. Thompson, J. Sheridan, and K. Hourigan, "A review of rotating cylinder wake transitions," J. Fluids Struct. **53**, 2–14 (2015).
[20]T. K. Sengupta and P. Deepak, "Flow past a circular cylinder executing rotary oscillation: Dimensionality of the problem," Phys. Fluids **30**(9), 093602 (2018).
[21]W. Chen and C. K. Rheem, "Experimental investigation of rotating cylinders in flow," J. Mar. Sci. Technol. **24**, 111–122 (2019).
[22]J. Lin, H. D. Yao, Y. Han, Y. Su, and C. Zhang, "Shape optimization and hydrodynamic simulation of a Magnus anti-rolling device based on fully parametric modelling," Phys. Fluids **35**(5), 055136 (2023).
[23]Daichin and S. J. Lee, "Near-wake flow structure of elliptic cylinders close to a free surface: Effect of cylinder aspect ratio," Exp. Fluids **36**, 748–758 (2004).
[24]P. Reichl, K. Hourigan, and M. C. Thompson, "Flow past a cylinder close to a free surface," J. Fluid Mech. **533**, 269–296 (2005).
[25]B. Bouscasse, A. Colagrossi, S. Marrone, and A. Souto-Iglesias, "SPH modelling of viscous flow past a circular cylinder interacting with a free surface," Comput. Fluids **146**, 190–212 (2017).
[26]S. Malavasi and A. Guadagnini, "Interactions between a rectangular cylinder and a free-surface flow," J. Fluid. Struct. **23**(8), 1137–1148 (2007).
[27]H. Ren, Y. Xu, M. Zhang, S. Deng, S. Li, S. Fu, and H. Sun, "Hydrodynamic forces on a partially submerged cylinder at high Reynolds number in a steady flow," Appl. Ocean Res. **88**, 160–169 (2019).
[28]F. Zhao, R. Wang, H. Zhu, H. Ping, Y. Bao, D. Zhou, Y. Cao, and H. Cui, "Large-eddy simulations of flow past a circular cylinder near a free surface," Phys. Fluids **33**(11), 115108 (2021).
[29]P. Kumar, A. K. Das, and S. K. Mitra, "Air entrainment driven by a converging rotational field in a viscous liquid," Phys. Fluids **29**(10), 102104 (2017).
[30]S. K. Panda and B. K. Rana, "Numerical simulation and analytical prediction on the development of entrained air filament caused by the combined effect of rotational field and free stream flow," Ind. Eng. Chem. Res. **61**(26), 9456–9473 (2022).
[31]T. Abramowicz-Gerigk, Z. Burciu, J. Jachowski, O. Kreft, D. Majewski, B. Stachurska, W. Sulisz, and P. Szmytkiewicz, "Experimental method for the measurements and numerical investigations of force generated on the rotating cylinder under water flow," Sensors **21**(6), 2216 (2021).
[32]P. Koukouvinis, M. Gavaises, O. Supponen, and M. Farhat, "Numerical simulation of a collapsing bubble subject to gravity," Phys. Fluids **28**(3), 032110 (2016).
[33]M. Ottersten, H.-D. Yao, and L. Davidson, "Tonal noise of voluteless centrifugal fan generated by turbulence stemming from upstream inlet gap," Phys. Fluids **33**(7), 075110 (2021).
[34]M. Kim, J. Lim, S. Kim, S. Jee, and D. Park, "Assessment of the wall-adapting local eddy-viscosity model in transitional boundary layer," Comput. Methods Appl. Mech. Eng. **371**, 113287 (2020).
[35]I. Rodriguez, O. Lehmkuhl, U. Piomelli, J. Chiva, R. Borrell, and A. Oliva, "LES-based study of the roughness effects on the wake of a circular cylinder from subcritical to transcritical Reynolds numbers," Flow, Turbul. Combust. **99**, 729–763 (2017).
[36]N. Arya and A. De, "Effect of grid sensitivity on the performance of wall adapting SGS models for LES of swirling and separating–reattaching flows," Comput. Math. Appl. **78**(6), 2035–2051 (2019).
[37]C. W. Hirt and D. N. Billy, "Volume of fluid (VOF) method for the dynamics of free boundaries," J. Comput. Phys. **39**(1), 201–225 (1981).
[38]K. Yokoi, "Efficient implementation of THINC scheme: A simple and practical smoothed VOF algorithm," J. Comput. Phys. **226**(2), 1985–2002 (2007).
[39]M. M. Karim, B. Prasad, and N. Rahman, "Numerical simulation of free surface water wave for the flow around NACA 0015 hydrofoil using the volume of fluid (VOF) method," Ocean Eng. **78**, 89–94 (2014).
[40]S. Mittal and B. Kumar, "Flow past a rotating cylinder," J. Fluid Mech. **476**, 303–334 (2003).
[41]A. Munir, M. Zhao, H. Wu, and L. Lu, "Numerical investigation of wake flow regimes behind a high-speed rotating circular cylinder in steady flow," J. Fluid Mech. **878**, 875–906 (2019).
[42]A. Colagrossi, G. Nikolov, D. Durante, S. Marrone, and A. Souto-Iglesias, "Viscous flow past a cylinder close to a free surface: Benchmarks with steady, periodic and metastable responses, solved by meshfree and mesh-based schemes," Comput. Fluids **181**, 345–363 (2019).
[43]S. Park, G. Oh, S. H. Rhee, B. Y. Koo, and H. Lee, "Full scale wake prediction of an energy saving device by using computational fluid dynamics," Ocean Eng. **101**, 254 (2015).
[44]Y. Su, J. Lin, D. Zhao, C. Guo, and H. Guo, "Influence of a pre-swirl stator and rudder bulb system on the propulsion performance of a large-scale ship model," Ocean Eng. **218**, 108189 (2020).
[45]Recommended Procedures and Guidelines, "Uncertainty analysis in CFD verification and validation, methodology and procedures," in ITTC Proceedings of the 28th International Towing Tank Conference, 2017.
[46]A. Radi, M. C. Thompson, A. Rao, K. Hourigan, and J. Sheridan, "Experimental evidence of new three-dimensional modes in the wake of a rotating cylinder," J. Fluid Mech. **734**, 567–594 (2013).
[47]Navrose, J. Meena, and S. Mittal, "Three-dimensional flow past a rotating cylinder," J. Fluid Mech. **766**, 28–53 (2015).
[48]T. Tang, H. Zhu, J. Song, B. Ma, and T. Zhou, "The state-of-the-art review on the wake alteration of a rotating cylinder and the associated interaction with flow-induced vibration," Ocean Eng. **254**, 111340 (2022).